INTERNATIONAL JOURNAL FOR NUMERICAL METHODS IN FLUIDS
Int. J. Numer. Meth. Fluids 2006; **50**:817–844
Published online 30 September 2005 in Wiley InterScience (www.interscience.wiley.com). DOI: 10.1002/fld.1079

A continuous sensitivity equation method for time-dependent incompressible laminar flows

H. Hristova[1,‡,‖], S. Étienne[1,§,**], D. Pelletier[1,*,†,††] and J. Borggaard[2,¶,‡‡]

[1]*Génie mécanique, École Polytechnique de Montréal, Montréal, Qué., Canada H3C 3A7*
[2]*Interdisciplinary Center for Applied Mathematics Virginia Tech, Blacksburg, VA 24061-0531, U.S.A.*

SUMMARY

This paper presents a general sensitivity equation method (SEM) for time dependent incompressible laminar flows. The formulation accounts for complex parameter dependence and is suitable for a wide range of problems. The SEM formulation is verified on a problem with a closed form solution. Systematic grid convergence studies confirm the theoretical rates of convergence in both space and time. The methodology is then applied to pulsed flow around a square cylinder. The flow starts with symmetrical vortex shedding then transitions to the traditional Von Karman street (alternate vortex shedding). Simulations indicate that the transition phase manifests itself earlier in the sensitivity fields than in the flow field itself. Sensitivities are then demonstrated for fast evaluation of nearby flows and uncertainty analysis. Copyright © 2005 John Wiley & Sons, Ltd.

KEY WORDS: sensitivity equations; time-dependent flows; incompressible flows; Navier–Stokes; sensitivity analysis; uncertainty analysis; nearby solutions

1. INTRODUCTION

An engineer using CFD for design must answer two questions: are the flow predictions obtained with CFD accurate enough for design purposes? and what are the consequences

*Correspondence to: D. Pelletier, Génie mécanique, École Polytechnique de Montréal, C.P. 6079, succursale Centre-ville, Montréal (Québec), Canada H3C 3A7.
†E-mail: Dominique.Pelletier@polymtl.ca
‡E-mail: Hristina.Hristova@polymtl.ca
§E-mail: Stephane.Etienne@polymtl.ca
¶E-mail: jborggaard@vt.edu
‖Graduate Student.
**Research Fellow.
††Professor and Canada Research Chair.
‡‡Associate Professor.

Contract/grant sponsor: National Science and Engineering Council of Canada
Contract/grant sponsor: Canada Research Chair Program
Contract/grant sponsor: Fonds Québécois de Recherche Nature et Technologie
Contract/grant sponsor: Air Force Office of Scientific Research; contract/grant number: AFOSR F49620-00-1-0299

Received 22 June 2004
Revised 20 July 2005
Accepted 23 July 2005

of changing the parameters controlling the system (boundary conditions, shape parameters, etc.)? This paper presents a general continuous sensitivity equation method for time-dependent incompressible laminar flows as a means of answering the latter question.

The former issue is best dealt with by systematic time-step and grid refinement studies in a numerical analysis process called verification [1] which proceeds in two steps: code verification followed by simulation verification. Code verification ensures, through grid refinement studies, that the discretization algorithm delivers the theoretical rate of convergence on problems with a closed form solution. Simulation verification entails grid error estimation and grid refinement studies to assess a simulation's accuracy and its grid convergence. Whenever possible verification is followed by validation which assesses the physical suitability of the mathematical model by comparing verified predictions to quality measurements. See Reference [1] for a thorough discussion.

A sensitivity is defined as the derivative of a dependent variable with respect to a model parameter. For the flow around an airfoil, $\partial u/\partial \alpha$ is the sensitivity of the velocity with respect to the airfoil angle of attack. It expresses how the velocity field responds to perturbations of α around its nominal value. Sensitivity information can also provide fast evaluation of nearby flows without resorting to a full blown flow reanalysis. This is done via Taylor series in parameter space, and is especially useful to answer *what if questions* for complex flows. Finally, sensitivity information can serve to cascade input data uncertainty through a CFD code to yield uncertainty estimates of the flow response. In both cases speed and cost-effectiveness are achieved because sensitivities are obtained at a fraction of the cost of computing the flow.

There are several means of computing flow sensitivities: finite differences of flow solutions, the complex step method [2], automatic differentiation [3], and sensitivity equation methods (SEM) [4–6]. The first option is costly because the problem must be solved for two or more values of each parameter of interest. Furthermore, technical problems arise because non-matching meshes are obtained for different values of a shape parameter. The complex-step method is very effective. However, it requires a complete rewrite of the software in complex variables. While this can be automated, it has a significant impact on performance. Automatic differentiation is equivalent to differentiating the discrete equations to generate a system of equations for the discrete sensitivities. It is powerful because it automatically generates the code for calculating sensitivities. In many cases, implementation requires human intervention to ensure efficiency of the code.

Approaches to calculating sensitivities also differ depending on the order of the operations of approximation and differentiation. In the *discrete* sensitivity equation approach, the total derivative of the flow approximation with respect to the parameter is calculated [7], whereas in the *continuous* SEM one differentiates the continuum equations to yield differential equations for the continuous sensitivities [4]. See Reference [8] for a discussion of the two approaches. We have adopted the latter approach for several reasons. First, in the case of shape parameters, it avoids the delicate issue of computing mesh sensitivities. Second, because the continuous SEM works on the continuum equations, it avoids the issue of differentiating computational facilitators [9] such as upwind schemes in finite volume methods or stabilization terms in finite element formulations. Finally, the method has shown its robustness in optimization of noisy cost functions [10].

Sensitivity analysis is a more advanced field in solid mechanics than in fluid dynamics. Indeed, textbooks have been written on sensitivity analysis of structures [7, 8]. To our knowledge there is only one book on sensitivity analysis of flow problems [5]. It is recent and

more specialized than structural mechanics books. Also, Gunzburger [9] discusses sensitivity analysis in the context of flow control and optimization.

Automatic differentiation for first-order flow sensitivities is discussed by Sherman [11] and Putko [3]. Continuous SEMs may be found in References [4, 12–15] for aerodynamics applications. Application to heat conduction is reported by Blackwell [16]. Sensitivities for incompressible flows with heat transfer may be found in several References [6, 17–19]. Sensitivity analysis for turbulence models is detailed in the works by Godfrey [13] and by Turgeon [20, 21]. A wide variety of flow regimes were treated by the authors [6, 18, 19, 21–23]. This body of work has shown that sensitivities provide an enriched base of information on which to develop an understanding of complex flow problems and gain insight into the flow physics. The work presented here is an extension, to time-dependent flows, of the methodology developed previously for steady state flows [6, 19].

The paper is organized as follows. First, we present the equations describing time-dependent laminar flow along with their boundary and initial conditions. The sensitivity equations and their boundary/initial conditions are then described in detail. The methodology and its finite element solver are verified on a problem possessing a closed form solution. Finally, we apply the approach to pulsed flow around a square cylinder. Several uses of sensitivities are demonstrated. The paper ends with conclusions.

2. FLOW EQUATIONS

2.1. Navier–Stokes equations

The flow regime of interest is modelled by the momentum and continuity equations

$$\tilde{\rho}\frac{\partial \tilde{\mathbf{u}}}{\partial \tilde{t}} + \tilde{\rho}\tilde{\mathbf{u}} \cdot \tilde{\nabla}\tilde{\mathbf{u}} = -\tilde{\nabla}\tilde{p} + \tilde{\mathbf{f}} + \tilde{\nabla} \cdot [\tilde{\mu}(\tilde{\nabla}\tilde{\mathbf{u}} + (\tilde{\nabla}\tilde{\mathbf{u}})^{\mathrm{T}})] \tag{1}$$

$$\tilde{\nabla} \cdot \tilde{\mathbf{u}} = 0 \tag{2}$$

where $\tilde{\rho}$ is the density, $\tilde{t}$ is the time, $\tilde{\mathbf{u}}$ is the velocity, $\tilde{p}$ is the pressure, $\tilde{\mu}$ is the viscosity, and $\tilde{\mathbf{f}}$ is a body force. The tilde $\sim$ denotes dimensional quantities.

The above system is closed with a proper set of initial conditions

$$\tilde{\mathbf{u}}(\tilde{\mathbf{x}}, \tilde{t} = 0) = \tilde{\mathbf{U}}_0(\tilde{\mathbf{x}}) \quad \text{in } \Omega \tag{3}$$

and Dirichlet and Neumann boundary conditions

$$\tilde{\mathbf{u}}(\tilde{\mathbf{x}}, \tilde{t}) = \tilde{\mathbf{U}}_{\mathrm{b}}(\tilde{\mathbf{x}}, \tilde{t}) \quad \text{on } \Gamma_{\mathrm{D}} \tag{4}$$

$$\tilde{\mathbf{t}} = [-\tilde{p}\mathbb{I} + \tilde{\mu}(\tilde{\nabla}\tilde{\mathbf{u}} + \tilde{\nabla}\tilde{\mathbf{u}}^{\mathrm{T}})] \cdot \hat{\mathbf{n}} = \tilde{\mathbf{F}}^{\mathrm{N}} \quad \text{on } \Gamma_{\mathrm{N}} \tag{5}$$

where Ω is the computational domain, $\tilde{\mathbf{U}}_{\mathrm{b}}$ is the value of the velocity imposed on the boundary Γ_{D}, $\mathbb{I}$ is the identity tensor, and $\tilde{\mathbf{F}}^{\mathrm{N}}$ is the boundary value of the surface traction force $\tilde{\mathbf{t}}$ imposed on the boundary segment Γ_{N}, and $\hat{\mathbf{n}}$ is the outward unit normal to Γ_{N}.

We make the equations dimensionless by selecting reference quantities for all variables and physical properties: $\tilde{L}_0$, $\tilde{\rho}_0$, $\tilde{\mu}_r$, $\tilde{U}_r$, $\tilde{p}_r = \tilde{\rho}_r \tilde{U}_r^2$ and $\tilde{f}_r = \tilde{\rho}_r \tilde{U}_r^2 / \tilde{L}_r$. This leads to the following dimensionless variables:

$$x = \frac{\tilde{x}}{\tilde{L}_r}, \quad y = \frac{\tilde{y}}{\tilde{L}_r}, \quad u = \frac{\tilde{u}}{\tilde{U}_r}, \quad v = \frac{\tilde{v}}{\tilde{U}_r}$$

$$p = \frac{\tilde{p}}{\tilde{p}_r}, \quad \rho = \frac{\tilde{\rho}}{\tilde{\rho}_r}, \quad \mu = \frac{\tilde{\mu}}{\tilde{\mu}_r}$$

For constant property flows we have $\rho = 1$ and $\mu = 1$. Boundary conditions are normalized in the same manner. This leads to the following dimensionless continuity and momentum equations:

$$\rho \frac{\partial u}{\partial t} + \rho \mathbf{u} \cdot \nabla \mathbf{u} = -\nabla p + \mathbf{f} + \nabla \cdot \left[\frac{\mu}{Re} (\nabla \mathbf{u} + (\nabla \mathbf{u})^{\mathrm{T}}) \right] \tag{6}$$

$$\nabla \cdot \mathbf{u} = 0 \tag{7}$$

with initial conditions

$$\mathbf{u}(\mathbf{x}, t = 0) = \mathbf{U}_0(\mathbf{x}) \quad \text{in } \Omega \tag{8}$$

and Dirichlet and Neumann boundary conditions

$$\mathbf{u}(\mathbf{x}, t) = \mathbf{U}_{\mathrm{b}}(\mathbf{x}, t) \quad \text{on } \Gamma_{\mathrm{D}} \tag{9}$$

$$\mathbf{t} = [-p\mathbb{I} + \mu(\nabla \mathbf{u} + \nabla \mathbf{u}^{\mathrm{T}})] \cdot \hat{\mathbf{n}} = \mathbf{F}^{\mathrm{N}} \quad \text{on } \Gamma_{\mathrm{N}} \tag{10}$$

3. SENSITIVITY EQUATIONS

3.1. General formulation of sensitivity equations

The continuous sensitivity equations (CSE) are derived formally by implicit differentiation of the flow equations (6) and (7) with respect to an arbitrary model parameter a. We treat the variable $\mathbf{u}$ as a function of both space and of the parameter a. This dependence is denoted as $\mathbf{u}(\mathbf{x}; a)$. Defining the flow sensitivities as the partial derivatives $\mathbf{s}_u = \partial \mathbf{u} / \partial a$ and $s_p = \partial p / \partial a$, and denoting the derivatives of the fluid properties and other flow parameters by a ($'$), differentiation of Equations (6) and (7) yields

$$\rho' \frac{\partial \mathbf{u}}{\partial t} + \rho \frac{\partial \mathbf{s}_u}{\partial t} + \rho' \mathbf{u} \cdot \nabla \mathbf{u} + \rho \mathbf{s}_u \cdot \nabla \mathbf{u} + \rho \mathbf{u} \cdot \nabla \mathbf{s}_u = -\nabla s_p + \mathbf{f}' + \nabla \cdot [\mu'(\nabla \mathbf{u} + (\nabla \mathbf{u})^{\mathrm{T}}) + \mu(\nabla \mathbf{s}_u + (\nabla \mathbf{s}_u)^{\mathrm{T}})]$$

$$\nabla \cdot \mathbf{s}_u = 0$$

3.2. Initial and boundary conditions

Initial conditions for the sensitivity equations are obtained by implicit differentiation of Equations (8)

$$\mathbf{s_u}(\mathbf{x}, t=0) = \frac{\partial \mathbf{U}_0}{\partial a}(\mathbf{x}) \quad \text{in } \Omega \tag{11}$$

Dirichlet conditions are obtained in a similar manner. However, one must account for the fact that the boundary segment Γ_D may now depend on a. Thus, we write

$$\mathbf{u}(x_b(a), y_b(a); a) = \mathbf{U}_b(x_b(a), y_b(a); a) \tag{12}$$

so that one must take the total derivative on both sides to obtain a Dirichlet boundary condition for $\mathbf{s_u}$

$$\mathbf{s_u}(\mathbf{x}, t; a) = \frac{\mathrm{d}\mathbf{U}_b}{\mathrm{d}a}(\mathbf{x}, t; a) - \frac{\partial \mathbf{u}}{\partial x}\frac{\partial x_b}{\partial a} - \frac{\partial \mathbf{u}}{\partial y}\frac{\partial y_b}{\partial a} \quad \text{on } \Gamma_D \tag{13}$$

The first term on the right-hand side expresses the dependence of $\mathbf{U}_b$ on a, while $\partial x_b/\partial a$ and $\partial y_b/\partial a$ are the shape sensitivities of the boundary segment. They vanish if a is a value parameter. Note that the flow gradient multiplies $\partial x_b/\partial a$ and $\partial y_b/\partial a$. Thus, accurate boundary conditions for a shape parameter require accurate evaluation of the flow gradients at the boundary, a challenging task because accuracy of flow derivatives decreases near boundaries. Duvigneau has developed promising techniques for extracting accurate flow gradients at the boundary [24, 25].

As an example, consider the case of an inlet channel of height a delivering a constant flow rate, $\dot{\mathscr{V}}$ m^2/s in 2-D, to a plenum independently of the value of a as shown on Figure 1. We have

$$x_b = 0$$

$$y_b = ar$$

$$U_b = \frac{6r(1-r)}{a}\dot{\mathscr{V}} \quad r \in [0, 1]$$

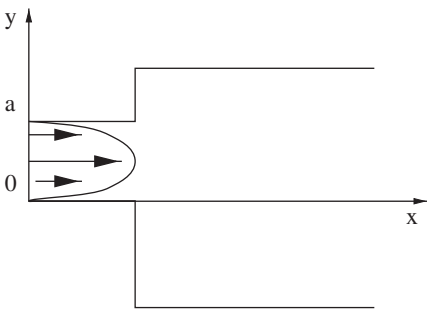

Figure 1. Plenum geometry.

where r is the parametric variable along the boundary and a is the model parameter. For this case the coefficients of Equation (13) are

$$\frac{\partial x_b}{\partial a} = 0$$

$$\frac{\partial y_b}{\partial a} = r$$

$$\frac{d\mathbf{U}_b}{da} = -\frac{6r(1-r)}{a^2}\dot{\mathscr{V}}$$

so that the boundary condition for s_u is

$$s_u = -\frac{6r(1-r)}{a^2}\dot{\mathscr{V}} - \frac{\partial u}{\partial y}r$$

If a increases, the channel becomes wider and the inflow velocities decrease accordingly to maintain a constant flow rate at the inlet.

For a value parameter the geometry of the domain does not depend on a. Hence, $\partial x_b/\partial a$ and $\partial y_b/\partial a$ vanish so that the boundary condition reduces to

$$\mathbf{s_u}(\mathbf{x}, t; a) = \frac{\partial \mathbf{U}_b}{\partial a}(\mathbf{x}, t; a) \quad \text{on } \Gamma_D \tag{14}$$

Neumann boundary conditions for the sensitivity of the surface forces $\mathbf{s_t} = \partial \mathbf{t}/\partial a$ given by

$$\mathbf{s_t} = [-s_p \mathbb{I} + \mu(\nabla \mathbf{s_u} + \nabla \mathbf{s_u}^T) + \mu'(\nabla \mathbf{u} + \nabla \mathbf{u}^T)] \cdot \hat{\mathbf{n}} + [-p\mathbb{I} + \mu(\nabla \mathbf{u} + \nabla \mathbf{u}^T)] \cdot \hat{\mathbf{n}}' \tag{15}$$

are obtained by implicit differentiation of Equation (10)

$$\mathbf{s_t} = \frac{d\mathbf{F}^N}{da} - \{-\nabla p \cdot \mathbf{\Pi}_b \mathbb{I} + \nabla \mu \cdot \mathbf{\Pi}_b(\nabla \mathbf{u} + \nabla \mathbf{u}^T) + \mu \mathbf{A}\} \cdot \hat{\mathbf{n}} \tag{16}$$

in which

$$\mathbf{\Pi}_b = \left(\frac{\partial x_b}{\partial a}, \frac{\partial y_b}{\partial a}\right)^T$$

and the components of the matrix $\mathbf{A}$ are

$$a_{11} = 2\left\{\frac{\partial^2 u}{\partial x^2}\frac{\partial x_b}{\partial a} + \frac{\partial^2 u}{\partial x \partial y}\frac{\partial y_b}{\partial a}\right\}$$

$$a_{12} = \left\{\frac{\partial^2 u}{\partial x \partial y}\frac{\partial x_b}{\partial a} + \frac{\partial^2 u}{\partial y^2}\frac{\partial y_b}{\partial a}\right\} + \left\{\frac{\partial^2 v}{\partial x^2}\frac{\partial x_b}{\partial a} + \frac{\partial^2 v}{\partial x \partial y}\frac{\partial y_b}{\partial a}\right\}$$

$$a_{21} = a_{12}$$

$$a_{22} = 2\left\{\frac{\partial^2 v}{\partial x \partial y}\frac{\partial x_b}{\partial a} + \frac{\partial^2 v}{\partial y^2}\frac{\partial y_b}{\partial a}\right\}$$

Note that both boundary conditions (13) and (16) require the evaluation of first or second derivatives of the flow at the wall. This constitutes an important challenge for the SEM as numerical differentiation results in reduced accuracy of the boundary conditions and hence, of the sensitivity solution also. Extracting accurate derivatives remains an open research question, although some progress has been made [24, 25]. In the case of a value parameter, all geometric derivatives vanish and Equation (16) yields the following simplified Neumann conditions:

$$\mathbf{s_t} = \frac{\partial \mathbf{F}^{\mathrm{N}}}{\partial a}(\mathbf{x}, t; a) \quad \text{on } \Gamma_{\mathrm{N}}$$

4. IMPLEMENTATION

The flow equations and the CSE are solved by a Galerkin finite element method. Time is discretized by an implicit Euler or a Crank–Nicholson scheme. The equations are linearized with Newton's method and discretized with the 7-node element using an enriched quadratic polynomial for the velocity and a piecewise discontinuous linear approximation of pressure. The same element is used to solve the sensitivity equations. Element matrices are constructed using a numerical Jacobian technique and assembled in a skyline data structure. Global systems for the flow and sensitivities are solved by LU factorization because of its robustness. Iterative methods could be used in place of the LU factorization. This would not change the results; it would only affect the memory requirement and CPU time requirements. For large meshes this would lead to significant savings on both aspects.

5. NUMERICAL RESULTS

Two numerical experiments are performed. The first one uses the method of manufactured solution (MMS) to verify the temporal and spatial accuracy of the flow and sensitivity solvers [1]. The second example is devoted to sensitivity analysis of time-dependent pulsed flow around a square cylinder.

5.1. Verification

According to the definition of Roache [1], verification is the process of ensuring that the differential equations are solved correctly, making sure that the code delivers the appropriate spatial and temporal rates of convergence on a problem with a known solution. The MMS is used to develop such solution expressions. With an analytical solution at hand, one can compute the error of the finite element solution, and use grid refinement studies to determine the temporal and spatial rates of convergence produced by the algorithm implementation. Direct differentiation of the manufactured solution provides closed form expressions for the sensitivities. A grid convergence study is performed to assess the accuracy of the flow and sensitivity solutions. We use the following expressions for the velocity components taken from the Stommel ocean flow model [26]:

$$u(x, y) = \frac{\mathscr{F}}{R} \cos\left(\frac{\pi y}{b}\right) [C_1 \mathrm{e}^{k_1 x} + C_2 \mathrm{e}^{k_2 x} - 1] \tag{17}$$

$$v(x, y) = -\frac{b}{\pi}\frac{\mathscr{F}}{R} \sin\left(\frac{\pi y}{b}\right) [C_1 k_1 \mathrm{e}^{k_1 x} + C_2 k_2 \mathrm{e}^{k_2 x}] \tag{18}$$

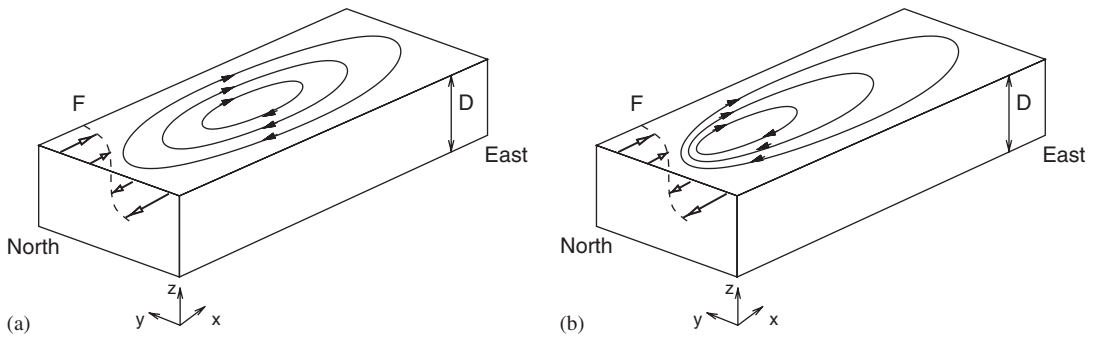

Figure 2. Flow pattern for ocean-like flow problem: (a) $\beta = 0$; and (b) $\beta \neq 0$.

with

$$k_{1,2} = -\frac{D\beta}{2R} \pm \sqrt{\left(\frac{D\beta}{2R}\right)^2 + \left(\frac{\pi}{b}\right)^2} \tag{19}$$

and

$$C_1 = \frac{1 - e^{k_2 \lambda}}{e^{k_1 \lambda} - e^{k_2 \lambda}}, \quad C_2 = \frac{e^{k_1 \lambda} - 1}{e^{k_1 \lambda} - e^{k_2 \lambda}} \tag{20}$$

Figures 2(a) and (b) are sketches of the flow field for $\beta = 0$ and $\beta \neq 0$. Also shown is the shape of the wind force $\mathscr{F}$. The original Stommel solution is for a steady-state flow. By taking

$$\mathscr{F} = F \sin(\pi t) \tag{21}$$

we generate a time-dependent velocity field suitable for verification. Finally, we choose the pressure to be

$$p(x, y) = 2\mu \frac{\partial v}{\partial y} = -2\frac{\mathscr{F}}{R} \cos\left(\frac{\pi y}{b}\right) [C_1 k_1 e^{k_1 x} + C_2 k_2 e^{k_2 x}] \tag{22}$$

so that a zero normal traction ($F_y^{\mathrm{N}} = 0$) in Equation (10) may be imposed on the top and bottom boundaries of the computational domain as shown in Figure 3. These expressions are substituted in the Navier–Stokes equations to define the body force $\mathbf{f}$ ensuring that the momentum equations (6) are satisfied. The meaning and values of the various parameters are given in Table I. For simplicity, the length scale is taken as $L^* = b = 2\pi \times 10^6$ m while the time-scale is $T^* = 1/\beta L^*$.

The computational domain and boundary conditions are shown on Figure 3. A grid and time-step convergence study is carried out for the flow and its sensitivities with respect to the following two parameters: the Coriolis coefficient β and the friction coefficient R. Analytical expressions for the sensitivities are obtained by direct differentiation of Equations (17)–(22). The required source term $\mathbf{f}'$ in the sensitivity equations is obtained by differentiation of $\mathbf{f}$ in Equation (6). The grid refinement study reported here is performed for $\beta = 0$. Similar results were obtained with $\beta \neq 0$. The mesh characteristics and time-step values used for

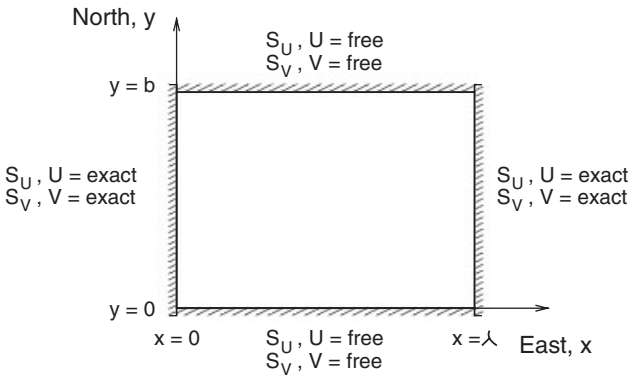

Figure 3. Domain for verification problem.

Table I. Parameters of the 'ocean-like' manufactured solution.

Parameter	Dimensional	Non-dimensional
Latitude, b	$2\pi \times 10^6$ m	1.00
Longitude, λ	10^7 m	1.59
Depth, D	200 m	3.1831×10^{-5}
Wind force, F	0.3×10^{-5} m^2 s^{-2}	1.9249×10^{-11}
Friction coefficient, R	0.6×10^{-3} m s^{-1}	1.5198×10^{-6}
Coriolis effect, β	10^{-11} m^{-1} s^{-1}	1.00

Table II. Mesh characteristics for verification problem.

	Mesh			Implicit Euler		Crank–Nicholson	
	N_{el}	N_{nodes}	h	$N_{\Delta t}$	Δt	$N_{\Delta t}$	Δt
1	48	117	0.2098	5	0.05	5	0.05
2	192	425	0.1049	20	0.0125	10	0.025
3	768	1617	0.05245	80	0.003125	20	0.0125
4	3072	6305	0.026225	320	0.00078125	40	0.00625

the verification problem are reported in Table II for the two schemes: first-order Euler and second-order accurate Crank–Nicholson time-stepping schemes. The meshes are unstructured grids of triangles of uniform size. The number of elements, nodes and the grid size h are given in the table along with the number of time-steps and time-step size required for integration of the unsteady Navier–Stokes equations from time $t = 0$ to 0.25. With this data one expects the true error evaluated at the final time of the simulation, to be reduced by a factor of 4 from one mesh to the next. This is achieved by setting

$$\frac{\Delta t}{h^2} = 1.1359$$

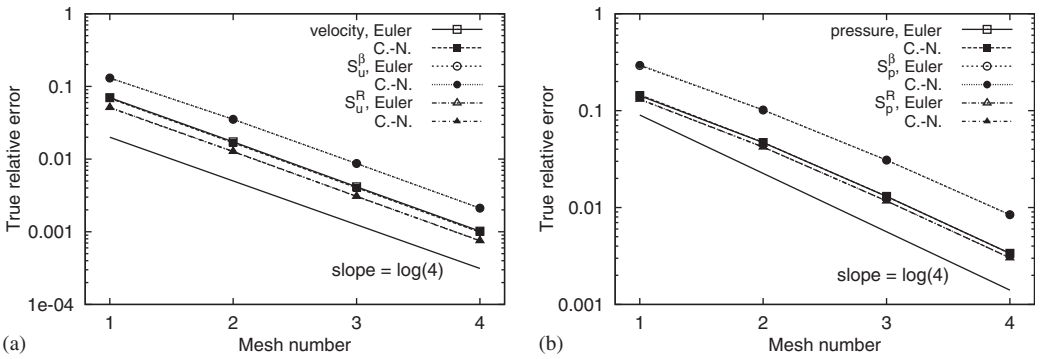

Figure 4. Verification problem: convergence of u, p and their sensitivities: (a) u and its sensitivities; and (b) p and its sensitivities.

for the Euler time integration scheme and

$$\frac{\Delta t}{h} = 0.2383$$

for the Crank–Nicholson time integrator. Notice that the time-step size diminishes with h much faster for the Euler scheme than the Crank–Nicholson scheme.

Figures 4(a) and (b) show the results for the velocity, the pressure and their sensitivities with respect to β and R. The spatial errors in velocity and pressure are measured at the end of the simulation (time $t = 0.25$). We use the energy norm for $\mathbf{u}$ and the L_2 norm for p

$$\|\mathbf{u}\|_E^2 = \int_\Omega [\nabla \mathbf{u} + (\nabla \mathbf{u})^{\mathrm{T}}] : [\nabla \mathbf{u} + (\nabla \mathbf{u})^{\mathrm{T}}] \, \mathrm{d}A \tag{23}$$

$$\|p\|_{L_2}^2 = \int_\Omega p^2 \, \mathrm{d}A \tag{24}$$

The colon represents the double contraction of two second-order tensors. For example, the double contraction of tensors $\mathbf{a}$ and $\mathbf{b}$ is computed as

$$\mathbf{a} : \mathbf{b} = \sum_i \sum_j \mathbf{a}_{ji} \mathbf{b}_{ij}$$

All error trajectories exhibit a slope of log(4) showing that the discretization schemes for the flow and sensitivity exhibit their theoretical rates of convergence: first-order in time for implicit Euler, and second-order accuracy for the implicit Crank–Nicholson scheme and second-order in space using norms given in Equations (23) and (24). Hence, the code is verified in the sense of Roache [1].

In the present case, the spatial error dominates over the temporal error. Thus the Euler and Crank–Nicholson schemes exhibit the same levels of spatial errors. Because the time-step to mesh size ratio is set to reduce both components (spatial and temporal) by a factor of 4, the trajectories of the global errors for the two time integration schemes lie on top of each

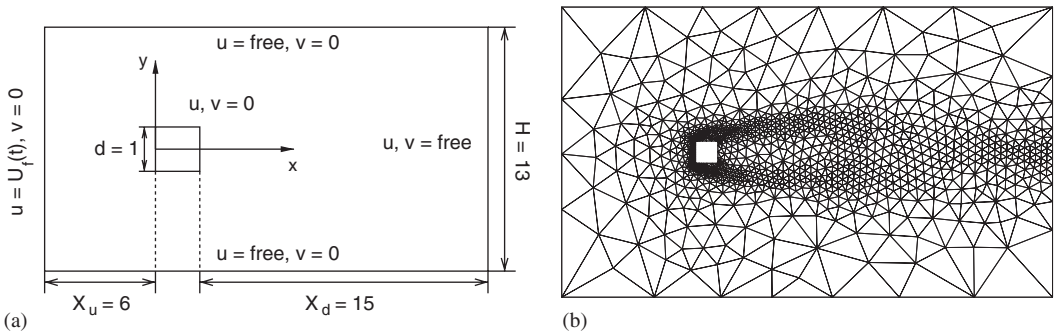

Figure 5. Definition and mesh for pulsed flow around a square cylinder: (a) domain and boundary conditions; and (b) mesh.

other. To better illustrate that the proper convergence rate is obtained, a reference line of slope log(4), corresponding to theory, is plotted. Note in Figure 4(b) that the error trajectories for pressure and its sensitivities deviate slightly from the theoretical slope between the first and second mesh. This simply indicates, that the grid resolution is not yet in the asymptotic range of the numerical scheme on the first mesh. The second mesh is likely in that range since the lines between meshes 2 and 3 are parallel to the reference theoretical solid line.

5.2. *Pulsed flow around a square cylinder*

5.2.1. Problem statement. The computational domain and boundary conditions for this problem are shown in Figure 5(a). The mesh is shown in Figure 5(b) and was designed to provide adequate flow and sensitivity resolution. All computations reported here were performed on this mesh. The inflow velocity varies in time according to

$$U_f(t) = U_0 \left(1 + \alpha \sin \frac{2\pi t}{T_\alpha}\right) \tag{25}$$

where U_0 is the time mean value of the free-stream velocity, α the amplitude of the sinusoidal variation, and T_α its period. These dimensionless parameters are set to

$$U_0 = 1, \quad \alpha = 0.4, \quad T_\alpha = 4 \tag{26}$$

The initial conditions are obtained from a steady-state solution of the flow and sensitivity equations. The Reynolds number $Re = \rho U_0 d/\mu$ is set to 100. Note that the mesh is adaptive with respect to steady-state velocity and pressure fields along with their sensitivities with respect to U_0. Parameters α and T_α only make sense in a time-dependent context. Hence, mesh adaptation on the steady-state initial conditions for sensitivities with respect to α and T_α cannot be done.

The time-step is set to $\Delta t = 0.025$ following the work of Sohankar [27]. This leads to 160 time-steps per period of the inflow boundary condition ($T_\alpha = 4$). Sensitivities are computed with respect to U_0, α, and T_α. The only non-zero boundary condition for the sensitivities are

those at the inlet. Implicit differentiation of U_f yields the following expressions at the inlet:

$$S_u^{U_0}(t) = \frac{\partial U_f}{\partial U_0} = 1 + \alpha \sin \frac{2\pi t}{T_\alpha} \tag{27}$$

$$S_u^{\alpha}(t) = \frac{\partial U_f}{\partial \alpha} = U_0 \sin \frac{2\pi t}{T_\alpha} \tag{28}$$

$$S_u^{T_\alpha}(t) = \frac{\partial U_f}{\partial T_\alpha} = U_0 \alpha \left(-\frac{2\pi t}{T_\alpha^2} \right) \cos \frac{2\pi t}{T_\alpha} \tag{29}$$

5.2.2. Flow response. The harmonic variation of the inflow boundary condition should induce symmetrical vortex shedding. This is exactly what is observed in Figure 6 which presents vorticity contours at various instants. Figure 7 shows the time variation of the inflow velocity and that of the flow (velocity and pressure) at a point located on the symmetry axis one diameter downstream of the cylinder ($x = 2, y = 0$). The signal is shown from time $t = 0$ for six periods of the inflow variation. Notice that the transverse velocity v is zero, confirming that the flow and vortex shedding are symmetric with respect to the x-axis. However, the v-component drifts slightly away from zero near $t = 20$, indicating that vortex shedding is no longer perfectly symmetrical. The axial velocity u and the pressure p vary with a period imposed by that of the inflow boundary condition. The streamwise velocity u is in phase with the inflow and corresponds to the variations induced by the shed vortices. Notice that the pressure is out of phase by $\pi/2$ with respect to the inflow. This phase shift is explained by looking at the mechanical energy equation (obtained by taking the dot product of the velocity with the momentum equations) and by integrating it over the computational domain

$$\frac{\mathrm{d}}{\mathrm{d}t} \int_\Omega \rho \frac{\mathbf{u}^2}{2} \, \mathrm{d}\Omega = \int_{\partial\Omega} \mathbf{u} \cdot (\boldsymbol{\sigma} \cdot \mathbf{n}) \, \mathrm{d}\Omega + \int_\Omega \boldsymbol{\tau} : \frac{1}{2} (\nabla \mathbf{u} + \nabla \mathbf{u}^{\mathrm{T}}) \, \mathrm{d}\Omega + \int_\Omega \mathbf{f} \cdot \mathbf{u} \, \mathrm{d}\Omega \tag{30}$$

where $\boldsymbol{\tau}$ is the stress tensor. Given the boundary conditions specified in Figure 5(a), the first term on the right-hand side reduces to a line integral along the inflow boundary. For simplicity, we assume that the work of viscous forces is small enough that the second integral can be neglected. Finally, the third integral also vanishes because there are no body forces. The kinetic energy equation then reduces to

$$\frac{\mathrm{d}}{\mathrm{d}t} \int_\Omega \rho \frac{\mathbf{u}^2}{2} \, \mathrm{d}\Omega = \int_{\text{inlet}} u t_x \, \mathrm{d}\partial\Omega \tag{31}$$

Now, away from the obstacle the flow is approximately equal to the inflow velocity so that the left-hand side takes the form

$$\frac{\mathrm{d}}{\mathrm{d}t} \int_\Omega \rho \frac{\mathbf{u}^2}{2} \, \mathrm{d}\Omega \approx \frac{\mathrm{d}}{\mathrm{d}t} \left(\rho \frac{U_f^2}{2} \mathrm{surf}(\Omega) \right) = \rho U_f \frac{\partial U_f}{\partial t} \mathrm{surf}(\Omega) \tag{32}$$

where $\mathrm{surf}(\Omega)$ is the surface area of the domain. The integral on the inlet of the domain can also be simplified to

$$u t_x = U_f \left(2\mu \frac{\partial U_f}{\partial x} - p \right) n_x = U_f \, p \tag{33}$$

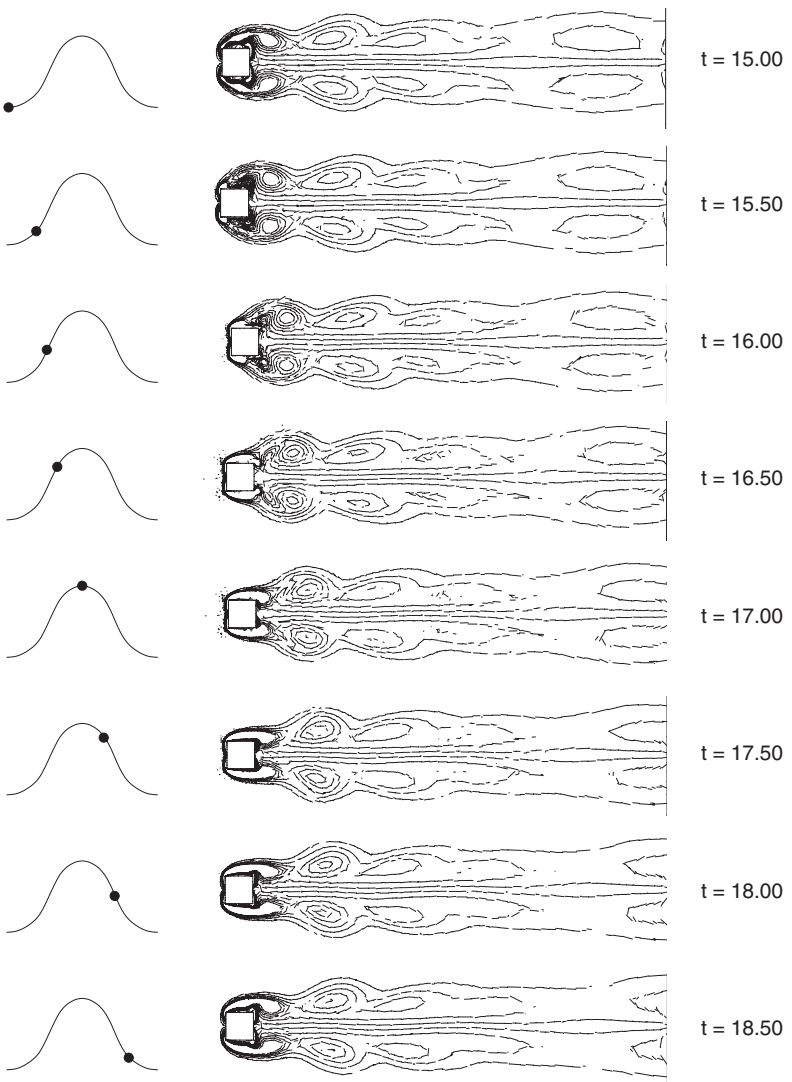

Figure 6. Symmetrical vortex shedding: vorticity contours.

This yields the following approximation for the pressure far from the obstacle:

$$p \approx x\rho \frac{\partial U_f}{\partial t} = x\rho\alpha U_0 \frac{2\pi}{T_\alpha}\left(\cos\frac{2\pi t}{T_\alpha}\right) \tag{34}$$

The cosine in the right-hand side explains the $\pi/2$ phase shift of the pressure with respect to the inflow velocity $U_f(t)$. The presence of the x term explains why the pressure contours are nearly vertical almost everywhere as seen on Figure 8. The contours are plotted at $t = 15$

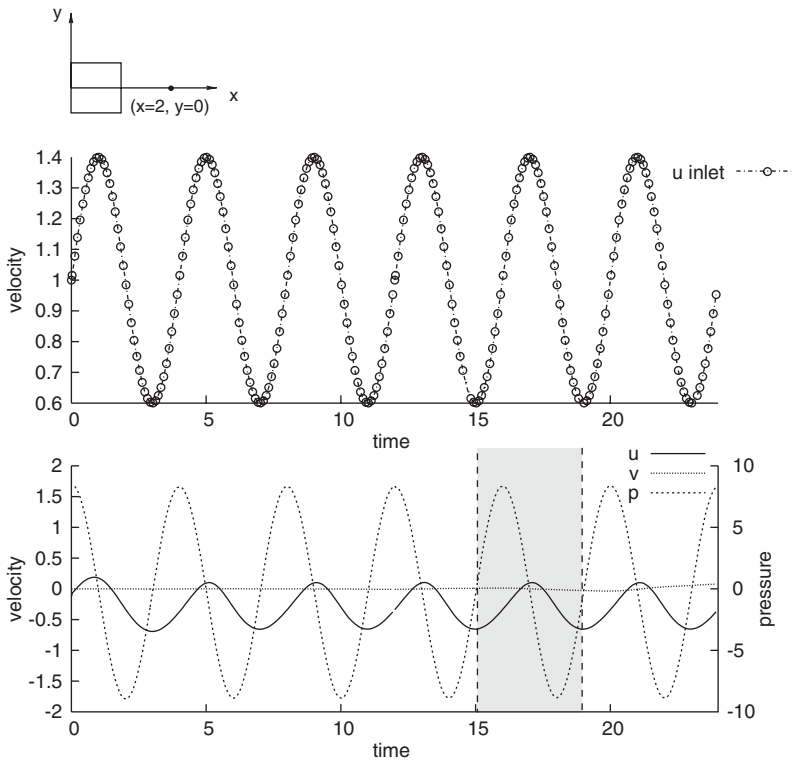

Figure 7. Flow response at $(x = 2, y = 0)$.

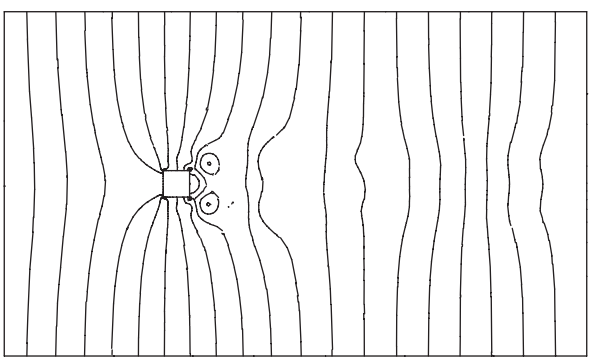

Figure 8. Pressure contours at $t = 15.0$.

which corresponds to the minimum of U_f. Perturbations to contours in the wake are due to the vortices travelling downstream from the obstacle.

To better visualize vortex shedding, vorticity contours are shown in Figure 6 over one period T_α corresponding to the shaded area on Figure 7. The points on the left-hand curves

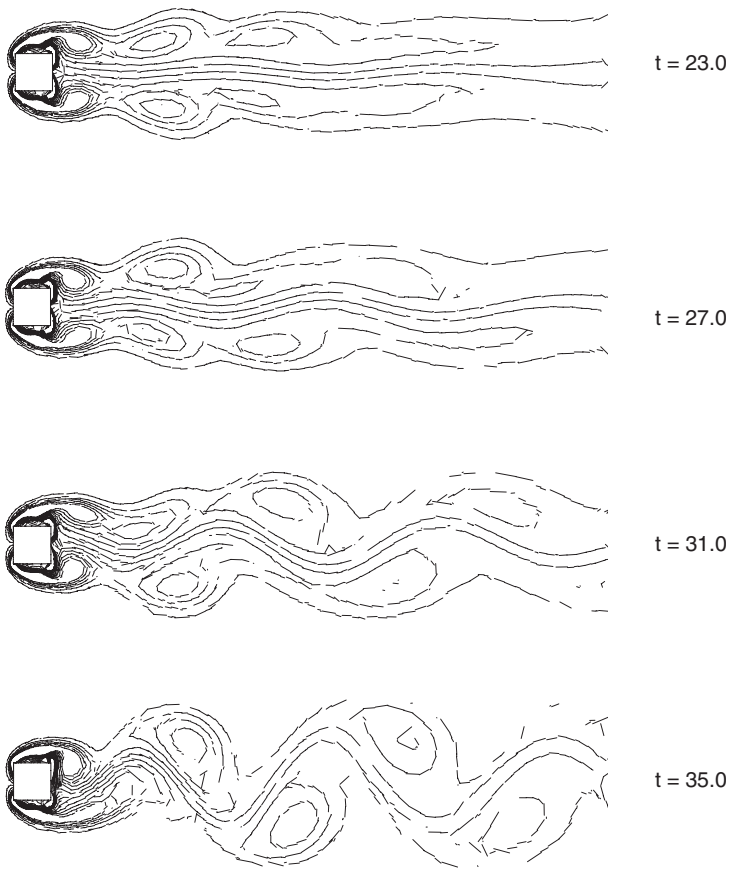

Figure 9. Karman vortex street at later times.

show the phase in the inflow boundary condition. Two vortices form at the rear corners of the square cylinder during the ascending phases of the pulsation and shedding occurs at the peak of the pulsation. Vortices are then transported downstream in the wake during the descending phase while two new vortices start building up. The flow remains symmetric throughout the flow period as can be seen from the straight contours near the symmetry axis. Thus, the dominant phenomena is symmetric vortex shedding induced by the flow pulsation.

By looking carefully at Figure 7 one notices that v deviates slightly from zero near the end of the simulation. A trend towards oscillation seems to be developing. The flow is no longer symmetric at time $t = 24$, an indication that a transition of flow regime is occurring. The simulation was continued for three additional periods T_α. Vorticity contours are shown on Figure 9 at times $t = 23$, 27, 31 and 35. The flow becomes strongly non-symmetric and a Karman vortex street is developing. This is to be expected as the wake of a square cylinder at $Re = 100$ is an unstable flow. Because the critical Reynolds number for this flow is $Re_{\text{cr}} = 51$

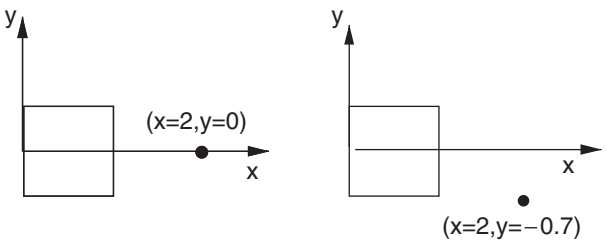

Figure 10. Location of points for extracting time signals.

[27], a vortex street would develop for constant inflow boundary conditions. Here, the pulsation at the inflow acts as a trigger for vortex shedding. Obviously, the final periodic flow will depend on T_α, the imposed pulsation period, and the obstacle natural shedding frequency.

5.2.3. Flow sensitivity responses. Time signals were extracted at two points located at $(x=2, y=0)$ on the symmetry axis and at $(x=2, y=-0.7)$ off the axis as shown in Figure 10. Time evolution of sensitivity signals, flow uncertainties, and fast nearby solutions will be shown at these points.

The time signal at $(x=2, y=0)$ of the flow sensitivities with respect to α, T_α and U_0 are shown on Figure 11. Figures are labelled as follows. The scale for the velocity sensitivities s_u and s_v is read on the vertical axis to the left while that for s_p is found on the vertical axis on the right-hand side of the plot. It should be obvious that velocity and pressure sensitivities have different units and that it is normal that they exhibit different magnitudes. Note that while the flow showed a harmonic response at nearly all times in the interval $[t=0, t=20]$, sensitivities show deviation from this behaviour at much earlier times than the flow itself. Deviation from symmetry in the flow signal appears at $t=22$ (Figure 7) while it occurs as early as $t=12$ for the sensitivities. See Figure 11. We note the following:

- the period of the sensitivity signals is T_α, the period of the inflow pulsation,
- for parameters α and U_0, the first period appears to be one of adjustment from the initial steady-state flow to the time-dependent regime,
- velocity and pressure sensitivities with respect to T_α exhibit linearly increasing amplitudes. This is to be expected since the inflow boundary condition for $S_u^{T_\alpha} = (-2\pi t U_0 \alpha / T_\alpha^2) \cos(2\pi t/T_\alpha)$ is a linearly increasing function of time,
- The most striking feature is the behaviour of the v-sensitivities. While initially small, they become sizable by the end of the simulation. This is especially visible for $S_v^{U_0}$ which becomes larger than $S_u^{U_0}$ by the end of the simulation. See Figure 11. A similar behaviour was observed in the time-signal of v, the transverse velocity component. This phenomenon starts sooner with the sensitivities and shows a more pronounced amplitude.
- Sensitivities appear able to foretell the transition from symmetrical to asymmetrical vortex shedding before it becomes visible in the flow signal.

The behaviour of the pressure sensitivities can be explained by differentiating the approximate expression for the pressure given in Equation (34). The behaviour of the sensitivities

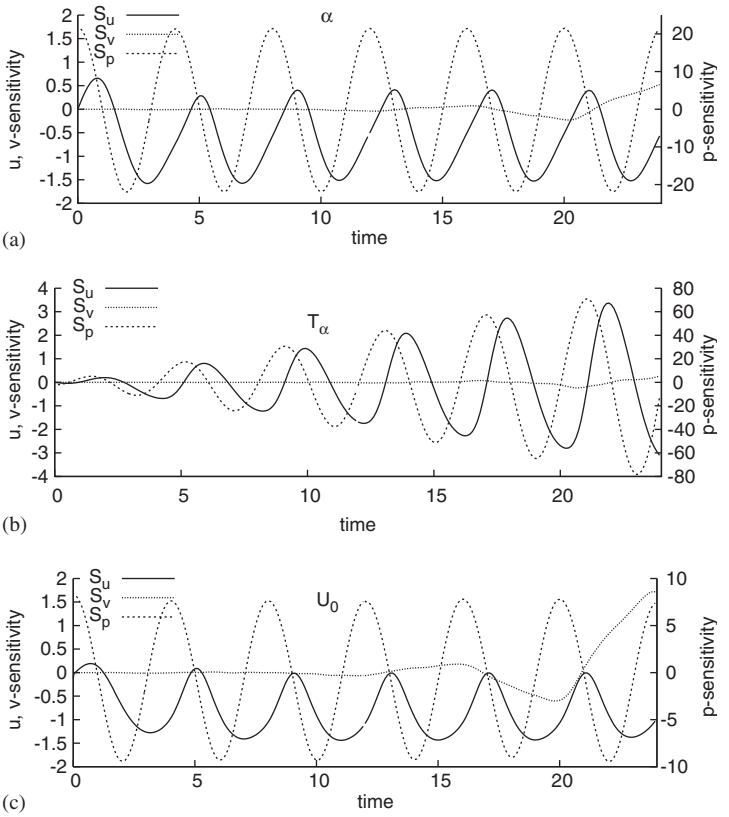

Figure 11. Time signal of sensitivities at $(x = 2.0, y = 0.0)$: (a) parameter $= \alpha$; (b) parameter $= T_\alpha$; and (c) parameter $= U_0$.

with respect to α and U_0 is similar to that of the pressure p

$$S_p^{\alpha} = \frac{\partial p}{\partial \alpha} \approx x\rho U_0 \frac{2\pi}{T_\alpha} \cos\left(\frac{2\pi t}{T_\alpha}\right)$$

$$S_p^{U_0} = \frac{\partial p}{\partial U_0} \approx x\rho\alpha \frac{2\pi}{T_\alpha} \cos\left(\frac{2\pi t}{T_\alpha}\right)$$

These are time-periodic harmonic variations of linear distributions in the streamwise direction.

The sensitivity with respect to T_α behaves differently

$$S_p^{T_\alpha} = \frac{\partial p}{\partial T_\alpha} \approx x\rho\alpha U_0 \frac{2\pi}{T_\alpha^2} \left[\frac{2\pi t}{T_\alpha} \sin\left(\frac{2\pi t}{T_\alpha}\right) - \cos\left(\frac{2\pi t}{T_\alpha}\right)\right] \tag{35}$$

The presence of the sine and cosine functions of time explain the phase shift compared to the other two sensitivities. Also, its amplitude increases with time due to the t multiplying the sine function.

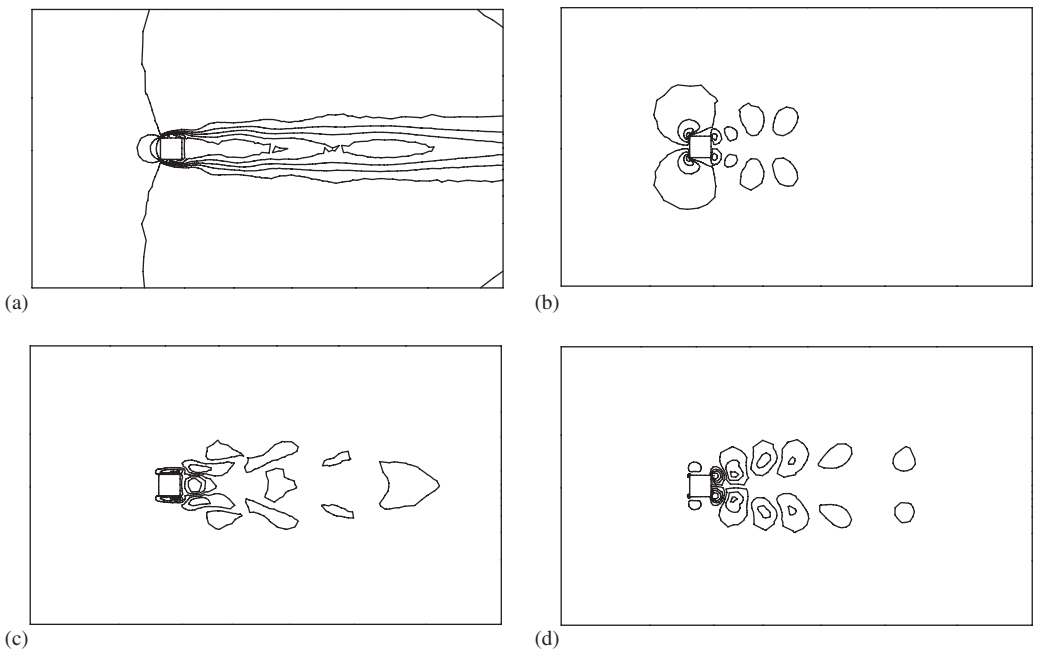

Figure 12. Flow and sensitivities at $t = 10$: (a) u; (b) v; (c) S_u^{α}; and (d) S_v^{α}.

We complete this section with a description of spatial distributions of the flow sensitivities. Figures 12 and 13 shows contours of u and v and their sensitivities with respect to α, U_0, and T_α at time $t = 10$ when the flow sensitivities are small according to Figure 11. Notice that all solution fields are symmetric. The sensitivities with respect to U_0 exhibit the richest structure (Figures 13(a) and (b)). Indeed, changing U_0 amounts to changing the Reynolds number of the flow. The fields of $S_v^{U_0}$ presents islands of alternating positive and negative values corresponding to vortices in the wake. This plot indicates that increasing U_0 will increase the strength of the vortices and bring them closer to the wake centreline. As can be seen the thickness of the wake decreases.

Sensitivities with respect to U_0 and α exhibit similar structure in the sense that the effect of a perturbation of the parameter is felt mostly in the wake of the square cylinder. This is consistent as both parameters affect the magnitude of the inflow or equivalently that of the effective Reynolds number. Finally, the distributions of sensitivities to T_α are different (Figures 13(c) and (d)). The effects of T_α are confined to the vicinity of the cylinder because T_α determines the period of the pulsation and, hence, that of vortex shedding. Once shed, vortices are transported by the mean flow so that the wake shows little sensitivity to T_α.

5.2.4. Uncertainty analysis. We now use sensitivity information to perform uncertainty analysis of the flow. Uncertainties on U_0 and α are cascaded through the CFD simulation to yield uncertainty estimates of the velocity response. For simplicity we perform the uncertainty one parameter at a time. Consider, for example, what happens to the u-velocity, when generic

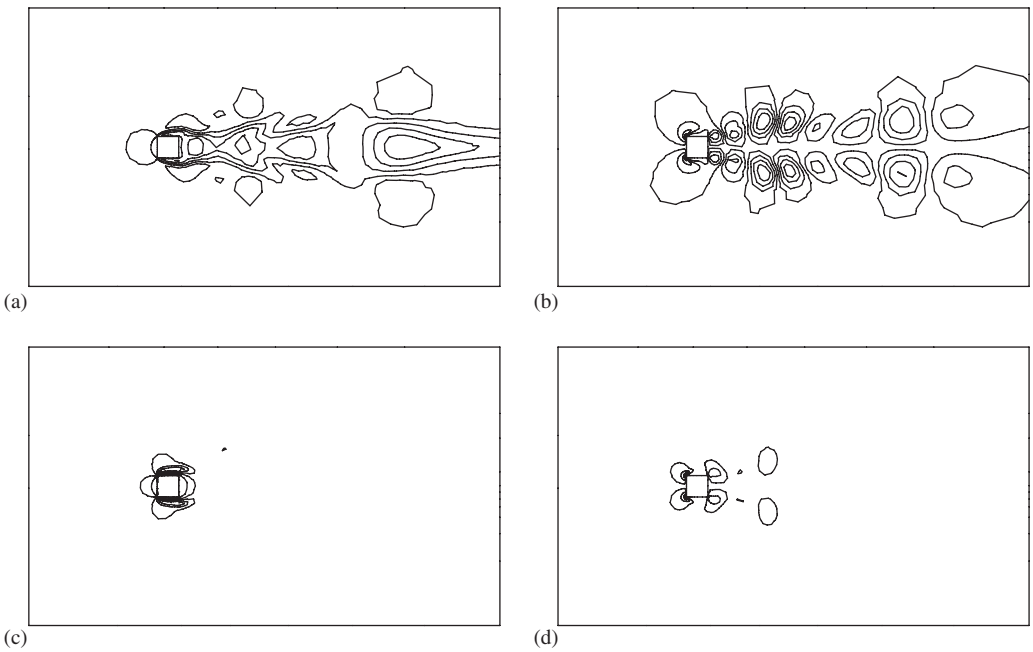

Figure 13. Sensitivities at $t = 10$: (a) $S_u^{U_0}$; (b) $S_v^{U_0}$; (c) $S_u^{T_\alpha}$; and (d) $S_v^{T_\alpha}$.

parameters a and b are subject to uncertainties δa and δb. The Taylor series are given by

$$u(x, y; a_0 + \delta a + \delta b) = u(x, y; a_0, b_0) + \frac{\partial u}{\partial a}\delta a + \frac{\partial u}{\partial b}\delta b$$

$$v(x, y; a_0 + \delta a + \delta b) = v(x, y; a_0, b_0) + \frac{\partial v}{\partial a}\delta a + \frac{\partial v}{\partial a}\delta a$$

which yields the following uncertainty estimates for u and v by the triangular inequality

$$\Delta u(x, y) \approx |S_u^a|\delta a + |S_u^b|\delta b \tag{36}$$

$$\Delta v(x, y) \approx |S_v^a|\delta a + |S_v^b|\delta b \tag{37}$$

Note that these expressions differ from those found in textbooks on experimental uncertainty analysis [28] which favour the use of RMS values

$$\Delta u(x, y) \approx [(S_u^a \delta a)^2 + (S_u^b \delta b)]^{1/2} \tag{38}$$

$$\Delta v(x, y) \approx [(S_v^a \delta a)^2 + (S_v^b \delta b)]^{1/2} \tag{39}$$

Both approaches are mathematically valid. Blackwell used Taylor series for uncertainty analysis [16] (i.e. Equations (36) and (37)). Note that Equations (36) and (37) yield bigger

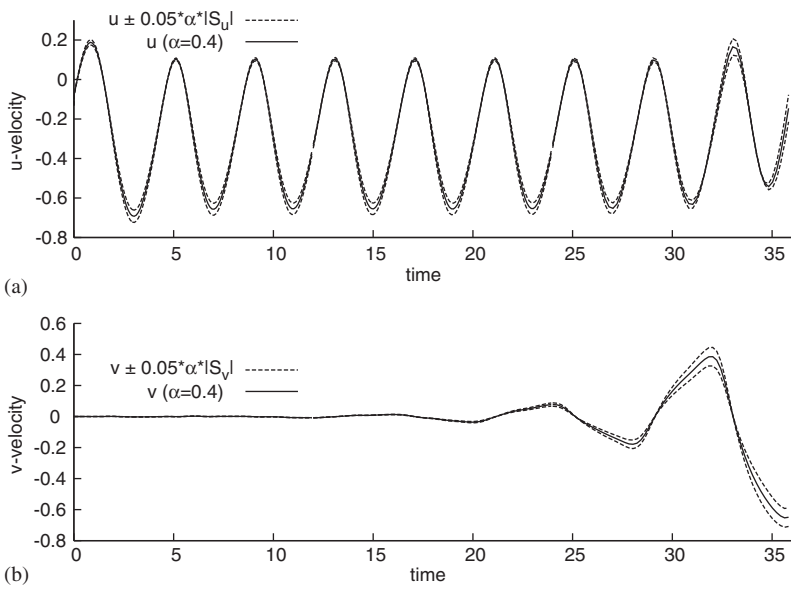

Figure 14. Uncertainty of flow response at $(x=2, y=0)$ for $\alpha = 0.4 \pm 0.02$ ($\Delta\alpha = 5\%$): (a) u and its uncertainty intervals $u \pm \delta u$; and (b) v and its uncertainty intervals $v \pm \delta v$.

(pessimistic) uncertainty estimates than expressions (38) and (39). However, the latter are more directly linked with statistical theories of uncertainty and uncertainty propagation. Note that the two approaches yield identical results if only one parameter is considered in the uncertainty analysis as is the case here.

We consider the following nominal values and uncertainties for parameters α and U_0:

$$\alpha = 0.4 \pm 0.02$$

$$U_0 = 1.0 \pm 0.02$$

This corresponds to 5% uncertainty on α and 2% on U_0. We propagate the uncertainty one parameter at a time for simplicity. That is for an arbitrary parameter we use the following formula:

$$\Delta u(x, y) \approx |S_u^a| \delta a$$

$$\Delta v(x, y) \approx |S_v^a| \delta a$$

Figures 14 and 15 present the velocity uncertainties induced by α while Figures 16 and 17 show those due to the uncertainty in the free stream velocity U_0. Results are given for two points in the domain. The first one is located on the symmetry axis of the obstacle $(x=2, y=0)$ so that v is small. The second point is offset in the transverse direction to a location $(x=2, y=-0.7)$ where v is larger. The equations of motion were integrated on a longer time interval $t=36$ (9 periods T_α instead of 6) to observe the behaviour of sensitivities

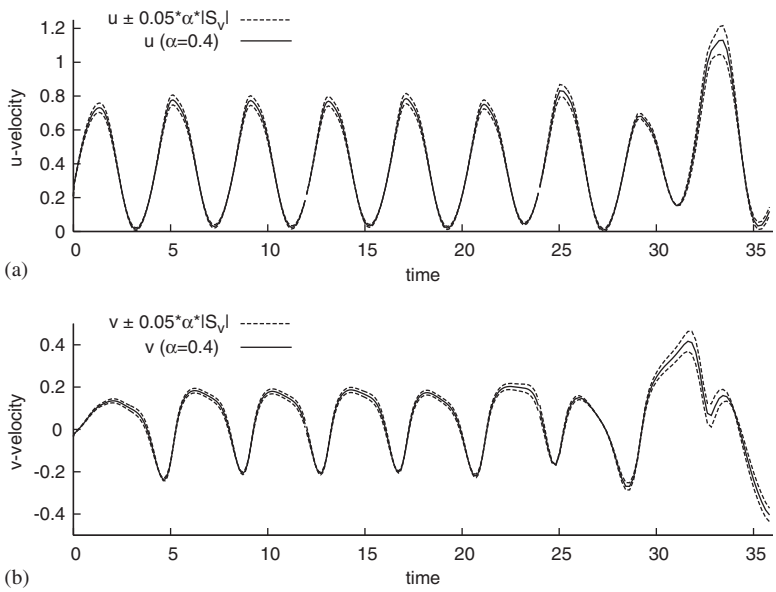

Figure 15. Uncertainty of flow response at $(x=2, y=-0.7)$ for $\alpha = 0.4 \pm 0.02$ ($\Delta\alpha = 5\%$): (a) u and its uncertainty intervals $u \pm \delta u$; and (b) v and its uncertainty intervals $v \pm \delta v$.

once the flow has undergone its transition to a Von Karman street. Note that there are three curves on each plot. The solid line is the time variation of the velocity component at the nominal value of the parameter ($\alpha = 0.4$ in Figures 14 and 15, $U_0 = 1.0$ in Figures 16 and 17). The two dashed lines represent the uncertainty bands $u(t) \pm \delta u(t)$ and $v(t) \pm \delta u(t)$.

As can be seen the uncertainties of the flow response are quite small until $t = 20$ (later for u). This is especially noticeable for v at the first point $(x=2, y=0)$. After $t = 20$, the uncertainty bands increase in magnitude. This behaviour is more pronounced in the case of the parameter U_0 (Figures 16 and 17) than for α (Figures 14 and 15). For $t > 30$, the uncertainties are so large that one may question the reliability of these estimates.

5.2.5. Fast evaluation of nearby flows. We now show how sensitivities can be used for fast evaluation of nearby flows. We use the above parameter perturbations in linear Taylor series and compare estimates of u and v to a full flow analysis at the perturbed values of the parameters. Results are shown in Figures 18 and 19 for perturbation of α and in Figures 20 and 21 for the case of a perturbation in U_0. We compare the following first-order Taylor series approximations for a generic parameter a

$$u(x, y; a_0 + \delta a) \approx u(x, y; a_0) + \frac{\partial u}{\partial a}\delta a \tag{40}$$

$$v(x, y; a_0 + \delta a) \approx v(x, y; a_0) + \frac{\partial v}{\partial a}\delta a \tag{41}$$

to a full blown simulation at the perturbed value of the parameter.

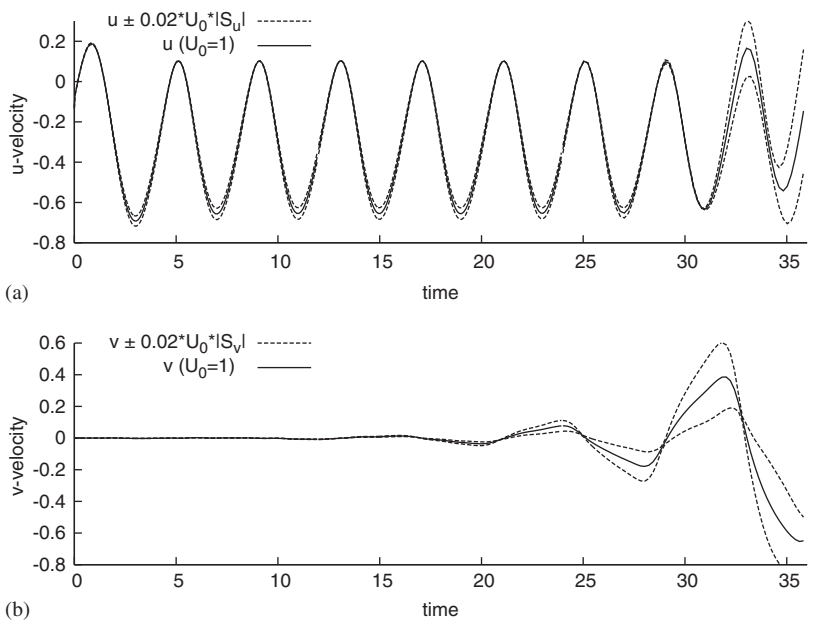

Figure 16. Uncertainty of flow response at $(x=2, y=0)$ for $U_0 = 1 \pm 0.02$ $(\Delta U_0 = 2\%)$: (a) u and its uncertainty intervals $u \pm \delta u$; and (b) v and its uncertainty intervals $v \pm \delta v$.

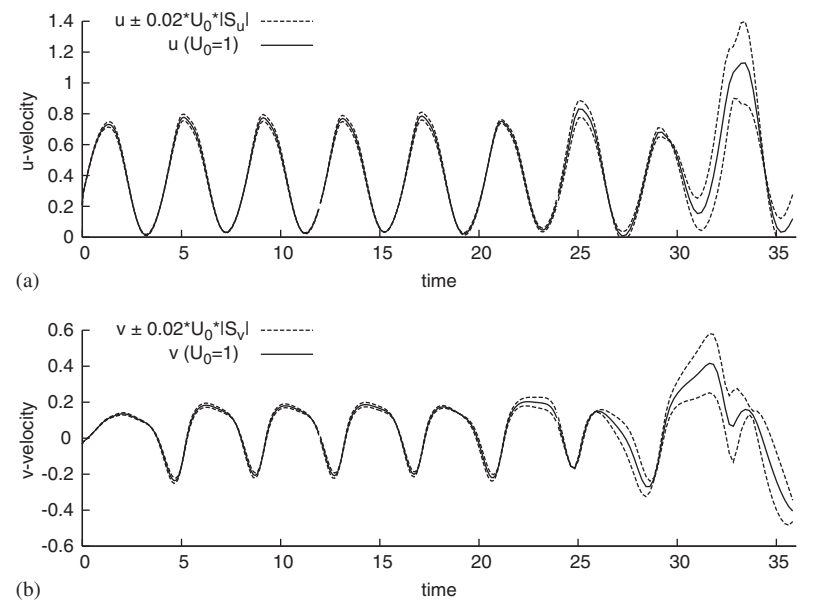

Figure 17. Uncertainty of flow response at $(x=2, y=-0.7)$ for $U_0 = 1 \pm 0.02$ $(\Delta U_0 = 2\%)$: (a) u and its uncertainty intervals $u \pm \delta u$; and (b) v and its uncertainty intervals $v \pm \delta v$.

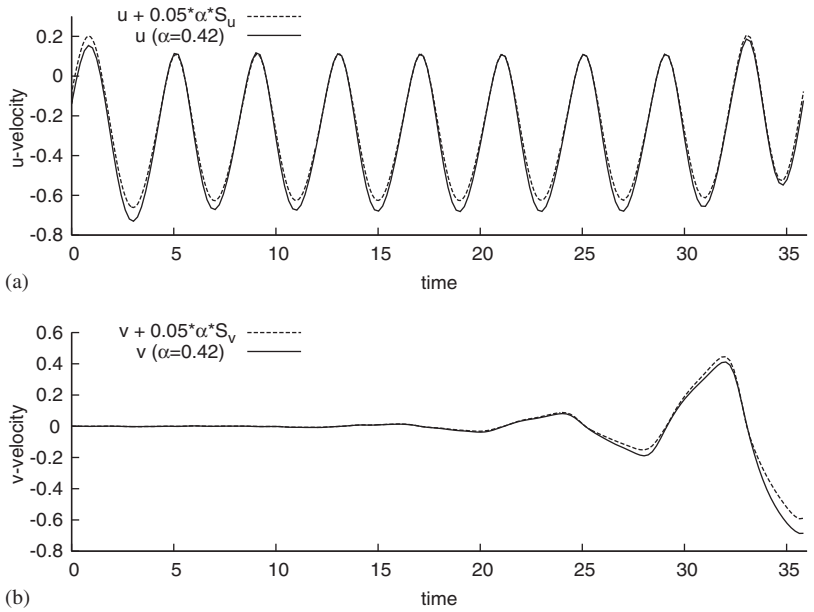

Figure 18. Fast nearby solution at $(x=2, y=0)$ for $\alpha=0.42$ ($\Delta\alpha=5\%$): (a) u-velocity; and (b) v-velocity.

There are two curves on each plot. The solid line represents the true response of the flow at the perturbed value of the parameter (full re-analysis): $\alpha=0.42$ for Figures 18 and 19; and $U_0=1.02$ for Figures 20 and 21. The dashed line is the flow response estimated using the linear Taylor series approximations (40) and (41). Figures 18 and 20 show the u and v response for a point on the symmetry axis at $(x=2, y=0)$ while Figures 19 and 21 are for a point off the axis at $(x=2, y=-0.7)$.

The Taylor series approximations of the flow response are in good agreement with the CFD analysis at the perturbed values of the parameters at early times, $t<20$. Agreement deteriorates at later times. Agreement is better for perturbations in α than for perturbations in U_0. In the latter case, the Taylor series still yields good results at early times. The Taylor series estimates are of poor quality for both u and v at later times when for $t>20$.

An interesting property of these sensitivities is worth mentioning. Both sensitivities $S_v^{U_0}$ and S_v^{α} at $(x=2, y=0)$ sense the transition from symmetric vortex shedding to a Von Karman vortex street much earlier than the flow and in a more pronounced fashion. Compare the signals for $S_v^{U_0}$ and S_v^{α} in Figures 18 and 20 to the signal of v on Figure 7. The departure from zero occurs near $t=22$ for v while it occurs at $t=12$ for $S_v^{U_0}$ and S_v^{α}. Again, flow sensitivities appear able to foretell the transition from symmetrical to asymmetrical vortex shedding before it becomes visible in the flow signal.

We end this section with a look at the spatial distributions of the velocity extrapolations obtained by Taylor series for parameter U_0 compared to those obtained by a full flow reanalysis. We use a fixed value of $\delta U_0=0.02$. Figure 22 compares the Taylor series extrapolation

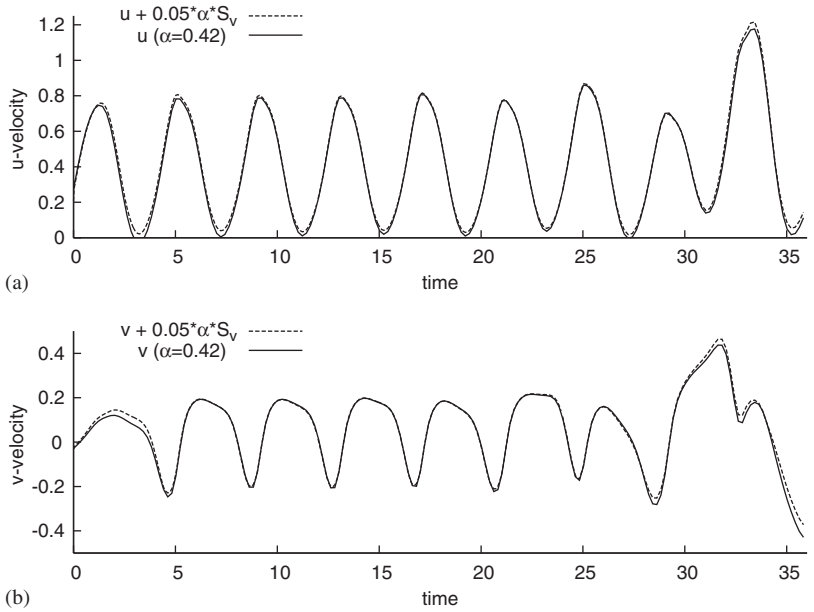

Figure 19. Fast nearby solution at $(x = 2, y = -0.7)$ for $\alpha = 0.42$ $(\Delta\alpha = 5\%)$: (a) u-velocity; and (b) v-velocity.

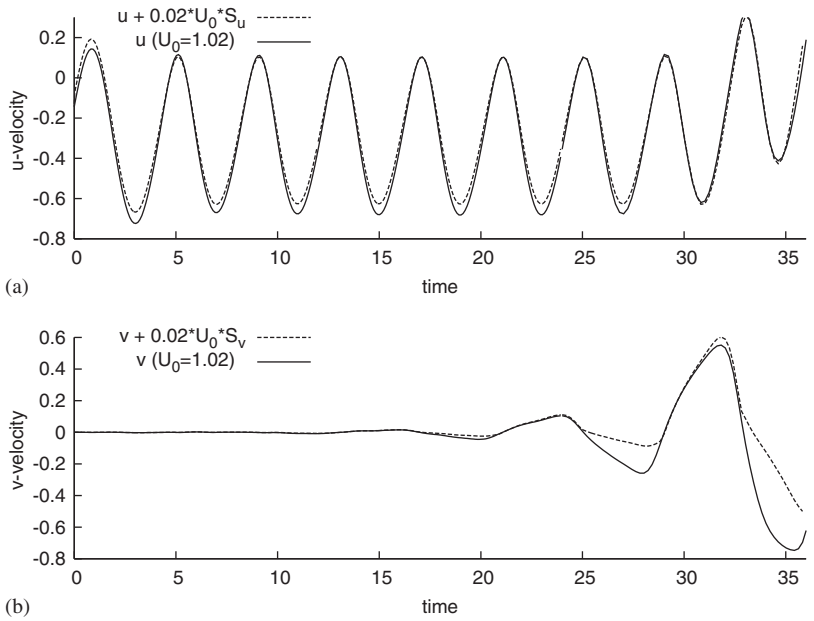

Figure 20. Fast nearby solution at $(x = 2, y = 0)$ for $U_0 = 1.02$ $(\Delta U_0 = 2\%)$: (a) u-velocity; and (b) v-velocity.

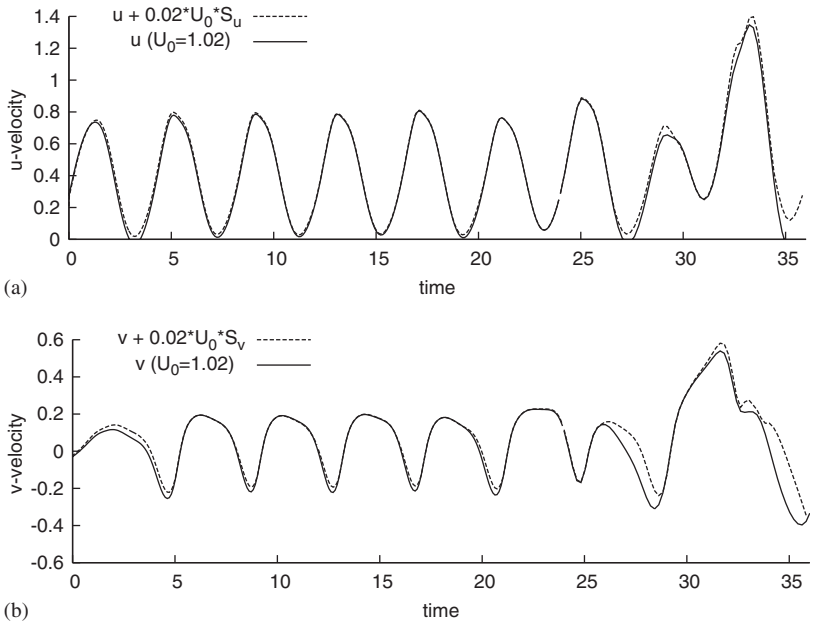

Figure 21. Fast nearby solution at $(x=2, y=-0.7)$ for $U_0=1.02$ ($\Delta U_0=2\%$): (a) u-velocity; and (b) v-velocity.

of v to that obtained by full reanalysis. The time value of $t=15$ corresponds to the minimum of the pulsation at the inflow while $t=17$ is at its peak. Comparisons are presented for stations located at $x=2$, 4 and 6. Generally speaking, Taylor series estimates are in better agreement with the true solution at time $t=17$ than at $t=15$. This is explained by the fact that the fixed perturbation $\delta U_0=0.02$ results in a smaller relative perturbation at the peak of the pulsation ($t=17$) than at its minimum ($t=15$). Recall that the inflow is given by

$$U_f(t)=U_0\left(1+\alpha\sin\frac{2\pi t}{T_\alpha}\right) \tag{42}$$

with $U_0=1$, $\alpha=0.4$, $T_\alpha=4$. Thus $U_{f_{\min}}=0.6$ and $U_{f_{\max}}=1.4$. Hence, the associated relative perturbations are 3% at $t=15$ and 1.4% at $t=17$. Note also that the agreement worsens with increasing downstream distance. This may be due in part to the coarser mesh in the downstream portion of the domain. Another possibility is the fact that streamwise distance can be interpreted as a time axis since the signal travels downstream with the flow. That is there is a time delay between the instant a particle of fluid passes through the station located at $x=2$ and and the time it goes by the station at $x=6$. The time delay being approximately $\Delta x/U_0=4$. The spatial discrepancies appear to be consistent with the time signature of the flow response as seen on Figure 21.

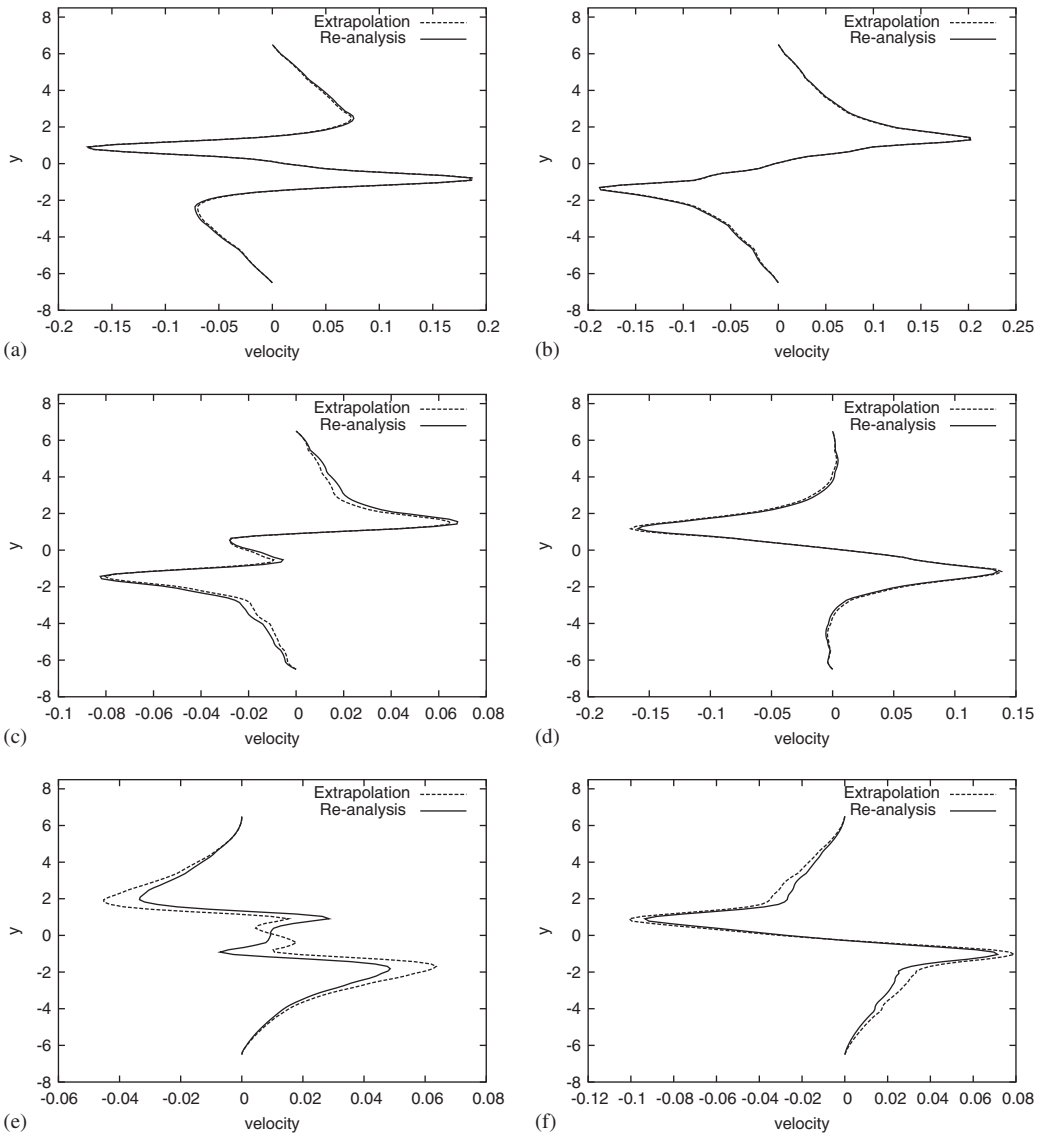

Figure 22. Extrapolated and true profiles of v: (a) $v(x=2,t=15)$; (b) $v(x=2,t=17)$; (c) $v(x=4,t=15)$; (d) $v(x=4,t=17)$; (e) $v(x=6,t=15)$; and (f) $v(x=6,t=17)$.

6. CONCLUSION

A general sensitivity equation formulation was developed for two-dimensional time-dependent incompressible laminar flows. The method was verified on a problem with a closed form solution to confirm the temporal and spatial rates of convergence of the solver. Results indicate

optimal convergence rates for both the flow and its sensitivities. This observation holds for both the Euler and Crank–Nicholson time-stepping schemes.

The method was applied to pulsed flow around a square cylinder. The flow starts with symmetrical vortex shedding due to the harmonic variation of the inflow boundary condition. The flow then goes through a transition phase leading to the well known Karman vortex street characterized by alternate vortex shedding. The flow sensitivities are especially sensitive to this flow transition. Indeed, signs of transition to asymmetrical vortex shedding appear much earlier in the sensitivity solution than in the flow variable themselves. This indicates that sensitivities are likely a very powerful tool to simulate and design optimal flow controllers. Sensitivities were also demonstrated as tool for uncertainty analysis and fast evaluation of nearby flows.

REFERENCES

1. Roache PJ. *Verification and Validation in Computational Science and Engineering*. Hermosa Publishers: Albuquerque, NM, 1998.
2. Martins JRRA, Stradza P, Alonso JJ. The complex-step derivative approximation. *ACM Transactions on Mathematical Software—TOMS* 2003; **29**(3):245–262.
3. Putko MM, Newman PA, Taylor AC, Green LL. Approach for uncertainty propagation and robust design in CFD using sensitivity derivatives. *15th AIAA Computational Fluid Dynamics Conference*. Anaheim: Brea, CA, June 2001, *AIAA Paper 2001-2528*.
4. Borggaard J, Burns J. A PDE sensitivity equation method for optimal aerodynamic design. *Journal of Computational Physics* 1997; **136**(2):366–384.
5. Stanley LG, Stewart DL. *Design Sensitivity Analysis*: *Computational Issues of Sensitivity Equation Methods*. Frontiers in Applied Mathematics, vol. 25. SIAM: Philadelphia, PA, 2001.
6. Turgeon É, Pelletier D, Borggaard J. A general continuous sensitivity equation formulation for complex flows. *8th AIAA/NASA/USAF/ISSMO Symposium on Multidisciplinary Analysis and Optimization*, Long Beach, CA, September 2000, *AIAA Paper 2000-4732*.
7. Haug EJ, Choi KK, Komkov V. *Design Sensitivity Analysis of Structural Systems*. Mathematics in Science and Engineering, vol. 177. Academic Press: Orlando, FL, 1986.
8. Kleiber M, Antúnez H, Hien TD, Kowalczyk P. *Parameter Sensitivity in Nonlinear Mechanics*. Wiley: New York, 1997.
9. Max D. Gunzburger. *Perspectives in Flow Control and Optimization*. SIAM: Philadelphia, PA, 2002.
10. Borggaard J, Pelletier D, Vugrin K. On sensitivity analysis for problems with numerical noise. *9th AIAA/ISSMO Symposium on Multidisciplinary Analysis and Optimization*, Atlanta, GA, September 2002. *AIAA Paper 2002-5553*.
11. Sherman LL, Taylor III AC, Green LL, Newman PA, Hou GW, Korivi VM. First- and second-order aerodynamic sensitivity derivatives via automatic differentiation. *Journal of Computational Physics* 1996; **129**(2):307–331.
12. Godfrey AG, Cliff EM. Direct calculation of aerodynamic force derivatives: a sensitivity-equation approach. *36th AIAA Aerospace Sciences Meeting and Exhibit*, Reno, NV, January 1998. *AIAA Paper 98-0393*.
13. Godfrey AG, Cliff EM. Sensitivity equations for turbulent flows. *39th AIAA Aerospace Sciences Meeting and Exhibit*, Reno, NV, January 2001. *AIAA Paper 2001-1060*.
14. Limache AC. Aerodynamic Modeling Using Computational Fluid Dynamics and Sensitivity Equations. *Ph.D. Thesis*, Virginia Polytechnic Institute and State University, Blacksburg, VA, 2000.
15. Turgeon É, Pelletier D, Borggaard J. Computation of airfoil flow derivatives using a continuous sensitivity equation method. *8th CASI Aerodynamics Symposium*, Toronto, Canada, April 2001.
16. Blackwell BF, Dowding KJ, Cochran RJ, Dobranich D. Utilization of sensitivity coefficients to guide the design of a thermal battery. *Proceedings of the 1998 ASME/IMECE*. Anaheim: Brea, CA, 1998; 73–82, *ASME. HTD-Vol. 561-5*.
17. Borggaard J, Pelletier D. Optimal shape design in forced convection using adaptive finite elements. *36th AIAA Aerospace Sciences Meeting and Exhibit*, Reno, NV, January 1998. *AIAA Paper 98-0908*.
18. Turgeon É, Pelletier D, Borggaard J. A general purpose sensitivity equation formulation for complex flows. *Proceedings of the 8th Annual Conference of the Computational Fluid Dynamics Society of Canada*, vol. 2, 11–13 June 2000, Montréal, Canada, 697–704.
19. Turgeon É, Pelletier D, Borggaard J. A continuous sensitivity equation method for flows with temperature dependent properties. *8th AIAA/NASA/USAF/ISSMO Symposium on Multidisciplinary Analysis and Optimization*, Long Beach, CA, September 2000. *AIAA Paper 2000-4821*.

20. Turgeon É, Pelletier D, Borggaard J. Application of a sensitivity equation method to the k–ε model of turbulence. *15th AIAA Computational Fluid Dynamics Conference*. Anaheim: Brea, CA, June 2001. *AIAA Paper 2001-2534*.
21. Turgeon É, Pelletier D, Borggaard J. A general continuous sensitivity equation formulation for the k–ε model of turbulence. *31st AIAA Fluid Dynamics Conference and Exhibit*. Anaheim: Brea, CA, June 2001. *AIAA Paper 2001-3000*.
22. Turgeon É, Pelletier D, Borggaard J. A continuous sensitivity equation approach to optimal design in mixed convection. *33rd AIAA Thermophysics Conference*, Norfolk, VA, June–July 1999. *AIAA Paper 99-3625*.
23. Turgeon É, Pelletier D, Borggaard J. Sensitivity and uncertainty analysis for variable property flows. *39th AIAA Aerospace Sciences Meeting and Exhibit*, Reno, NV, January 2001. *AIAA Paper 2001-0139*.
24. Duvigneau R, Pelletier D. Evaluation of nearby flows by a shape sensitivity equation method. *43rd AIAA Aerospace Sciences Meeting and Exhibit*, Reno, NV, January 2005. *AIAA Paper 2005-0127*.
25. Duvigneau R, Pelletier D. On accurate boundary conditions for a shape sensitivity equation method. *International Journal for Numerical Methods in Fluids* 2005, in press.
26. Von Schwind JJ. *Geophysical Fluid Dynamics for Oceanographers*. Prentice-Hall: Englewood Cliffs, NJ, 1980.
27. Sohankar A, Norberg C, Davidson L. Low-Reynolds-number flow around a square cylinder at incidence: study of blockage, onset of vortex shedding and outlet boundary condition. *International Journal for Numerical Methods in Fluids* 1998; **26**:39–56.
28. Hugh W, Coleman W, Glenn Steele Jr. *Experimentation and Uncertainty Analysis for Engineers*. Wiley: New York, 1989.

